

SVD-DIP: Overcoming the Overfitting Problem in DIP-based CT Reconstruction

Marco Nittscher*

MNITTSCH@UNI-BREMEN.DE

Center for Industrial Mathematics, University of Bremen, Germany

Michael Lameter*

LAMETER@UNI-BREMEN.DE

Center for Industrial Mathematics, University of Bremen, Germany

Riccardo Barbano

RICCARDO.BARBANO.19@UCL.AC.UK

Department of Computer Science, University College London, UK

Johannes Leuschner

JLEUSCHN@UNI-BREMEN.DE

Center for Industrial Mathematics, University of Bremen, Germany

Bangti Jin

B.JIN@CUHK.EDU.HK

Department of Mathematics, The Chinese University of Hong Kong, Shatin, N.T., Hong Kong

Peter Maass

PMAASS@UNI-BREMEN.DE

Center for Industrial Mathematics, University of Bremen, Germany

Abstract

The deep image prior (DIP) is a well-established unsupervised deep learning method for image reconstruction; yet it is far from being *flawless*. The *DIP overfits to noise* if not early stopped, or optimized via a regularized objective. We build on the regularized fine-tuning of a pretrained DIP, by adopting a novel strategy that restricts the learning to the adaptation of *singular values*. The proposed SVD-DIP uses *ad hoc* convolutional layers whose pretrained parameters are decomposed via the singular value decomposition. Optimizing the DIP then solely consists in the fine-tuning of the singular values, while keeping the left and right singular vectors fixed. We thoroughly validate the proposed method on real-measured μ CT data of a lotus root as well as two medical datasets (LoDoPaB and Mayo). We report significantly improved stability of the DIP optimization, by *overcoming the overfitting* to noise.

Keywords: Deep Image Prior, Fine-Tuning, Computed Tomography, Singular Value Decomposition

1. Introduction

In medical imaging, we are often interested in inverse problems of the form $y = Ax + \nu$, with $y \in \mathbb{R}^m$ being a noisy measurement, $x \in \mathbb{R}^n$ the unknown image of interest, A a linear forward operator, and $\nu \sim \mathcal{N}(0, \sigma^2 I)$ i.i.d. noise. This problem is often ill-posed, and regularization is needed to recover a sensible image (Engl et al., 1996; Ito and Jin, 2015).

In recent years, deep learning has been applied successfully to many imaging modalities, often via a supervised learning paradigm (Arridge et al., 2019; Ongie et al., 2020). However, supervised learning tends to require a large amount of paired training data to be effective (Bagger et al., 2020). Deep Image Prior (DIP) (Ulyanov et al., 2020) is an unsupervised alternative to applying deep learning to image reconstruction. Its main advantage over

* Contributed equally

supervised methods is that it requires no training data, and learns only on the observed data sample, relying on the rich structure of convolutional neural networks (CNNs) to have a regularizing effect on the image. However, it is not without limitations. The network can overfit to the noise, and has to be freshly trained for every image we intend to reconstruct. The Educated Deep Image Prior (EDIP) (Barbano et al., 2022) is a variant of DIP that addresses some of these issues. It uses pretraining by initializing the network architecture with a pretrained (warm-start) parameter setting, rather than randomly. However, EDIP still suffers from overfitting even if equipped with a regularized objective; iterating beyond a certain point leads to deteriorated quality.

The problem of overfitting is not unique to DIP. Recently, Sun et al. (2022) suggested a novel way of adapting pretrained parameters in a CNN using the singular value decomposition (SVD) to address overfitting and the generalization ability of a CNN specifically in the context of image segmentation. In this paper, our contribution is to integrate the idea of the SVD fine-tuning into the EDIP framework, achieving remarkable stability. Specifically, we first train a CNN on synthetic data, and before warm-starting the DIP with the pretrained parameter setting, we replace some or all of the layers of the network using the SVD. In our experiments, the resulting DIP (i.e., SVD-DIP) is much more resistant to overfitting. When iterating for very long, e.g. 200k iterations, it retains a high PSNR value, outperforming the classical DIP. Additionally, the SVD-DIP reports an almost non-existent drop in the maximal PSNR value.

2. The Deep Image Prior

Given a measurement y , the DIP (Ulyanov et al., 2020) finds an x that minimizes $\|Ax - y\|_2^2$. The method trains a CNN, typically deploying a U-Net architecture (Ronneberger et al., 2015), to fit to the single data sample (z, y) , where z is a randomly initialized input (e.g., with i.i.d. Gaussian noise). The DIP finds a parameter setting θ such that the output of the neural network $\varphi_\theta(z) = x$ minimizes the error $\|A\varphi_\theta(z) - y\|_2^2$. This requires training a CNN for each y ; the optimization can take hours or even days, depending on the complexity (esp. high-dimensionality) of the reconstruction task (Barbano et al., 2022). The method relies on the observation that the CNN structure already captures a sufficient amount of low-level image statistics, such that it can reconstruct an image well even without being trained on any data save for the input image (Dittmer et al., 2020). When data is scarce or expensive to acquire, this represents a major upside. However, the Achilles' heel of the DIP is overfitting to noise. When optimizing for too long, the network fits the noise. There are several approaches to alleviate this issue. The use of an explicit regularization term (Liu et al., 2018) is one of them. For all our DIP variants, we replace the standard objective used in Ulyanov et al. (2020) $\|A \cdot - y\|_2^2$ with

$$\|A \cdot - y\|_2^2 + \gamma \text{TV}(\cdot) \quad (1)$$

where $\gamma > 0$ and $\text{TV}(x) := \sum_{i,j} |x_{i+1,j} - x_{i,j}| + \sum_{i,j} |x_{i,j+1} - x_{i,j}|$ is the anisotropic total variation. That is, the DIP baseline uses the regularized objective in Equation 1. The latter only partially alleviates overfitting to the noise, often not being sufficient to prevent it completely. Other methods rely on the Stein's unbiased risk estimator (Jo et al., 2021) (also see Appendix E), or on hand-crafted early-stopping criteria (Liu et al., 2018; Wang

et al., 2021). Additionally, one may constrain the network to an under-parameterized regime such that its ability to fit to noise is reduced, e.g., deep decoder (Heckel and Hand, 2019).

The Educated Deep Image Prior (EDIP) (Barbano et al., 2022) is a variant of the DIP that makes use of pretraining, motivated by wanting to speed up the DIP, since freshly training DIP on multiple measurements is time-consuming. The idea is to first train the CNN architecture using available or synthetic data. The obtained parameter setting θ^* is used as the starting point for the subsequent DIP reconstructive task on y . This “warm-start” allows the network to reconstruct the desired image in fewer iterations, exploiting benign inductive biases learned in the pretraining phase.

3. Overcoming Overfitting via an SVD-based Pretrained CNN

While the original EDIP model was motivated by a desire to speed up the DIP, we are instead interested in utilizing pretraining to address overfitting. Intuitively, we can think of the warm-start parameter setting obtained via pretraining as a list of tensors W , each coding the weights for a convolutional layer in the CNN. In EDIP, this parameter setting is used as the initialization. Thus, the only mechanism in place to stop from eventually overfitting to noise is the TV term in the loss. Our approach, the SVD-DIP, integrates the idea from (Sun et al., 2022) of adapting the pretrained parameter setting, into the DIP framework. Specifically, the pretrained tensor $W \in \mathbb{R}^{C_{out} \times C_{in} \times K \times K}$ (which represents $K \times K$ convolutions) is first folded into a matrix $W' \in \mathbb{R}^{C_{out} \times C_{in} K^2}$. Then, the SVD yields three matrices, $U' \in \mathbb{R}^{C_{out} \times R}$, $S' \in \mathbb{R}^{R \times R}$ (diagonal), $V' \in \mathbb{R}^{R \times C_{in} K^2}$ ($R = \min\{C_{out}, C_{in} K^2\}$),

$$W' = U' S' V'.$$

These matrices can be “unfolded” back into three tensors $U \in \mathbb{R}^{C_{out} \times R \times 1 \times 1}$, $S \in \mathbb{R}^{R \times R \times 1 \times 1}$, $V \in \mathbb{R}^{R \times C_{in} \times K \times K}$ such that composing the tensors’ induced convolutions is equivalent to taking the original tensor’s induced convolution. For the technical details, see Appendix A. The key idea of the proposed approach is to represent the network parameters in this form, then freeze the tensors U and V , keeping their convolutions fixed, but allowing the tuning of the singular values (SVs), i.e. the diagonal of S' .

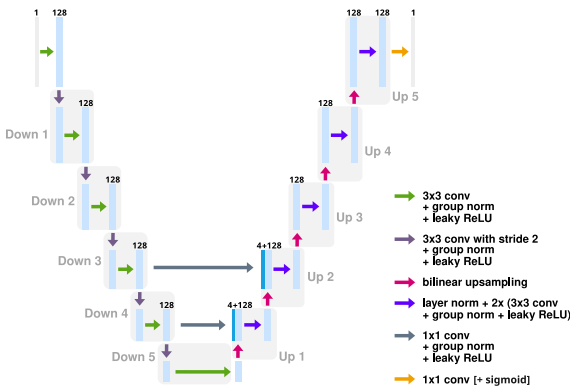


Figure 1: U-Net architecture used for experiments with pretraining on Ellipses.

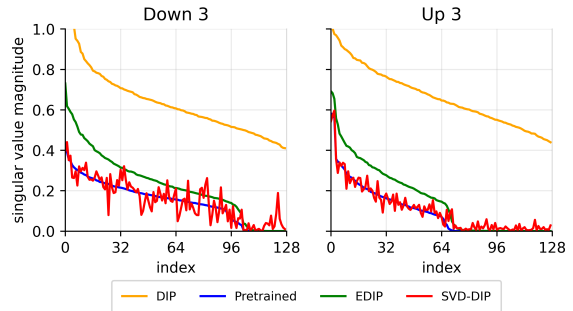


Figure 2: SVs taken from the 1st convolutions of Down layer 3 and Up layer 3 of the U-Net on the lotus.

Freezing U, V and only varying the SVs retains the structure learned by pretraining the network, but the weighting of these structural components can be fine-tuned for a specific task at hand: increasing the weight of more important structures, or reducing less important ones. Figure 2 shows that the SVs of the pretrained CNN are modified by SVD-DIP, but still retain the overall trend of the original values.

Prior to the DIP fine-tuning, the network encodes the same function whether it is warm-started with the pretrained parameter setting, or its SVD-adapted counterpart, since with or without the SVD replacement, each layer performs exactly the same convolutional operation. Once fine-tuning begins, the two methods diverge from each other with SVD-DIP being more constrained due to having fewer parameters. The way the SVD is used to replace convolutional layers can be viewed as parameter compression; if $C_{in} = C_{out}$, the number of SVs is a fraction of the square root of the number of parameters of the original tensor. This drastic reduction in the number of parameters, while still retaining enough expressive power thanks to the structure learned during pretraining being encoded in U and V , greatly alleviates the overfitting issue and stabilizes the convergence, as demonstrated by the experiments below. When constraining the parameter space, we sacrifice some capability to represent finer structure, but gain substantial robustness to overfitting. Here we are more interested in a proof of concept for a method with high stability, which bypasses the need for reliable early stopping criteria, even when the pretraining and application datasets are fairly different.

4. Experiments and Results

4.1. The Experiment Setup

We conduct our experiment on both pCT and medical CT image datasets. During pretraining, the U-Net learns to post-process filtered back-projections of noisy CT projections, that are simulated using the geometry of the target data. See Appendix B for more details. We consider the following scenarios:

Pretraining on Ellipses \rightarrow fine-tuning on Lotus and LoDoPaB’s Chest Pretraining is performed on a dataset consisting of synthetically generated ellipses, which is commonly used for inverse problems arising in imaging (Adler and Öktem, 2017) and used to warm-start DIP for CT reconstruction in (Barbano et al., 2022). Synthetic data is advantageous in applications where data is scarce. 5% Gaussian noise is added to the simulated projection data. We use this approach for two target datasets: (i) real-measured pCT data of a lotus root (Bubba et al., 2016) (fan-beam geometry with 20 angles, 429 detector pixels and image size $128 \times 128 \text{ px}^2$); (ii) simulated medical chest CT data from LoDoPaB (Leuschner et al., 2021) (parallel-beam geometry with 200 angles, 513 detector pixels and image size $362 \times 362 \text{ px}^2$). It is simulated to include Poisson noise corresponding to 4096 photons per pixel before attenuation. As per best practice, the ground truth images with low artifact corruption were preferred when selecting 10 LoDoPaB test samples via manual inspection before running any experiments. Note that there is a shift in noise distribution between pretraining that uses 5% Gaussian noise and the target data which is either real-measured or simulated to contain Poisson noise. The U-Net architecture is shown in Figure 1, as in (Barbano et al., 2022). The SVD replacements reduce the number of pa-

rameters from $128^2 \cdot 3^2$ to 128 in each convolution layer, i.e., reducing by a factor of $\frac{1}{1152}$. We refer to the two transfer settings as “Ellipses-Lotus” and “Ellipses-LoDoPaB”.

Pretraining on Chest \rightarrow fine-tuning on Mayo’s Head, Abdomen and Chest Pre-training is performed on LoDoPaB (Leuschner et al., 2021). The dataset contains ca. 40k chest CT images of size 362×362 px² and simulated parallel-beam projections with 1000 angles, 513 detector pixels and Poisson noise corresponding to 4096 photons per pixel before attenuation. We experiment with both the original 1000-angle geometry as well as a sub-sampled 200-angle geometry. We use images of different body parts from (Moen et al., 2021) as the images to be reconstructed and simulate observations using the same geometry and noise setting that was used in LoDoPaB. The used U-Net architecture is shown in Appendix B Figure 8(b). We refer to this setting as “LoDoPaB-Mayo”.

Then we use the resulting parameters as our pretrained parameters. Both EDIP and SVD-DIP receive the filtered back-projection obtained from test data, $z = \text{FBP}(y)$, matching the post-processing task of the pretraining, while DIP receives an i.i.d. Gaussian noise image z . For the target data containing Poisson noise (Ellipses-LoDoPaB and LoDoPaB-Mayo), we replace the squared error $\|A \cdot y - y\|_2^2$ in the objective (1) with the Poisson regression loss matching the noise distribution. A suitable regularization parameter γ is chosen for each setting, and the same value is used for all methods. See Appendix B for more details. We repeat three times for each image from the data sets, for each variant of DIP. We test the classical (randomly initialized) DIP, EDIP and SVD-DIP.

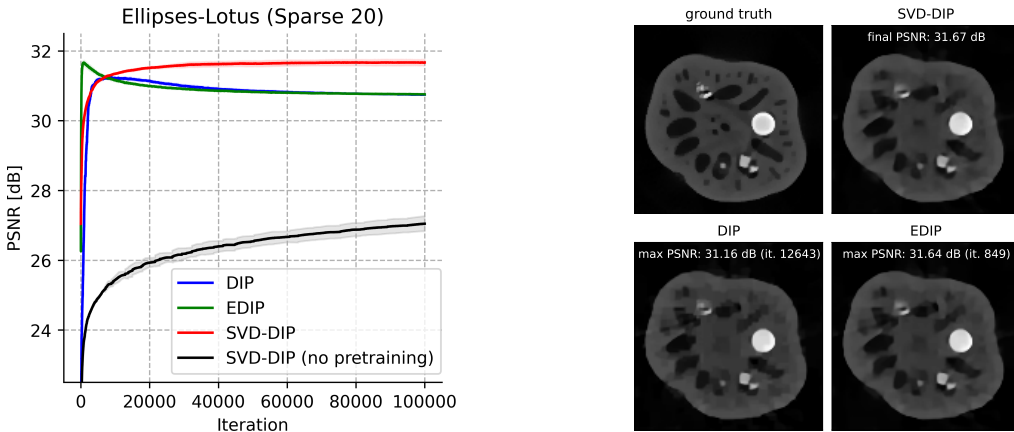


Figure 3: Optimization of DIP, EDIP and SVD-DIP on the lotus, pretraining on ellipses. Each line represents the mean over 3 runs, the colored area the standard deviation. The final SVD-DIP reconstruction is shown on the right, along with the max PSNR reconstructions of DIP and EDIP, which would require ideal early stopping.

4.2. Comparison of Methods

4.2.1. μ CT OF LOTUS ROOT (ELLIPSES-LOTUS)

Figure 3 shows the convergence behaviour of the different DIP frameworks for the lotus. EDIP peaks very early, attaining a maximum PSNR (max PSNR) value of 31.66 dB. However, after achieving the peak value, its PSNR steadily decreases, indicating insufficient regularization to prevent overfitting. The vanilla DIP is outperformed by the (pretrained) SVD-DIP in terms of the attained maximal PSNR, and is far less stable; its PSNR falls also after peaking, while the PSNR of SVD-DIP does not decline. The DIP also has a lower maximal PSNR. While EDIP has similar stability issues as DIP, it also has better max PSNR. Irrespective of the variant, or the performance metric, pretraining improves on the DIP for the lotus. After around 10k iterations, SVD-DIP and EDIP are at a similar PSNR, and after many more iterations, SVD-DIP reaches and marginally surpasses peak values of EDIP. Thus, the pretrained SVD-DIP performs as well as EDIP in terms of max PSNR and drastically outperforms EDIP in terms of stability (and thus, the PSNR of the final iteration). EDIP has the benefit of the speed at which it reaches its best PSNR value.

As an ablation study, we also include the results for SVD-DIP without pretraining, which performs much worse than the rest. This is not surprising, since it can only learn a weighting of the singular vectors possessing no useful structure, due to the random initialization. The SVD decomposition can't make use of its ability to compress information, so there is no reason to expect the randomly initialized SVD to be beneficial.

SVD Truncation Since before and after the fine-tuning, SVs close to zero generally remain so, we observe that the SVD-DIP can be further reduced in the number of parameters by the truncated SVD. Figure 4 contains a comparison of SVD-DIP settings with different approaches to truncation. For (50% rd.), we truncated all but the top 50% of the SVs. For (10% thresh.), we truncated all SVs which are below 10% of the largest SV. The graph shows that the different variations of SVD-DIP perform very similarly, the difference between their PSNRs being within one standard deviation of the SVD-DIP without truncation. Thus, the lotus root image is simple enough to allow for a low-dimensional representation of the parameter space by only the upper 50% of the SVs (50% rd.), or only the values greater or equal to 10% of the largest (10% thresh.). In this experiment, the truncated DIPs have reduced variance between runs, though this would need to be tested more rigorously. Other percentages, both for the threshold and the reduction approach, were tested, but generally performed worse or were on par with these.

4.2.2. CHEST CT (ELLIPSES-LoDoPAB)

DIP has a better max PSNR on average (see Table 1). SVD-DIP reaches on average a lower max PSNR than EDIP and DIP, but it is much more stable, with the PSNR trending upwards, rather than declining. Figure 5 exemplarily shows the behavior of the PSNR observed in the runs. On average, SVD-DIP outperforms DIP and EDIP, arriving at a slightly lower value in a remarkably stable manner. Thus, the strong regularization induced by fixing the singular vectors comes at the cost of a slightly lower max PSNR, but on the other hand greatly reduces the overfitting. Here, for SVD-DIP we replace the convolutional layers in all down- and up-blocks by SVD representations, except the first three down-blocks.

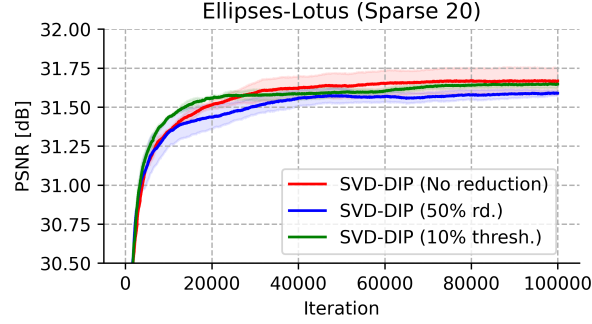


Figure 4: Optimization of SVD-DIP for forms of truncation on the lotus, pretraining on ellipses. Each line represents the mean over 3 runs, the colored area the SD.

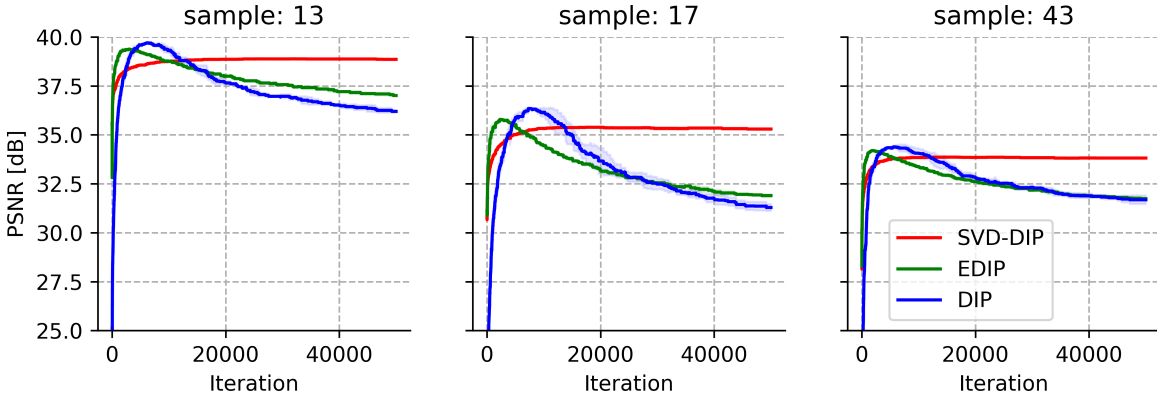


Figure 5: Optimization of DIP, EDIP and SVD-DIP on LoDoPaB (Sparse 200) test samples 13, 17 and 43, pretraining on ellipses. Each line represents the mean over 3 runs.

We can treat the number of down-blocks that remain unchanged as a hyperparameter, which can be adjusted depending on the need to adapt to different input data. For example, we replace fewer blocks here because we experience a major change in the noise distribution, and want to give the network more flexibility.

4.2.3. CT OF DIFFERENT BODY PARTS (LoDoPAB-MAYO)

As can be seen from Figure 6, SVD-DIP on average reports higher final PSNR values when compared to EDIP and DIP, as well as comparable max. PSNR values. While the DIP is shown to be stable in this setting, it does not outperform SVD-DIP in terms of final PSNR. EDIP performs the worst, as the PSNR falls off the most. This is due to the fact that the pretrained parameters are close to the optimal ones (i.e., high initial PSNR values), so that EDIP very quickly starts overfitting. Since EDIP and SVD-DIP start with the same pretrained parameters (modulo different representation), SVD-DIP also shows this behavior. However, the parameters are far more constrained, and thus the degree of overfitting is greatly by far reduced, allowing it to still outperform both EDIP and the DIP.

Table 1: Mean PSNR values for Ellipses-LoDoPaB (Sparse 200) over 3 runs and 10 images, 50000 Iterations each. Max denotes the maximum PSNR, Final denotes the PSNR attained after 50000 iterations. Values are in dB. Table 4 in the Appendix contains the data for all runs on which we compute the mean.

	DIP		Pretraining	EDIP		SVD-DIP	
	Final	Max	Init	Final	Max	Final	Max
Mean	32.08	35.34	30.51	32.39	35.09	34.65	34.76

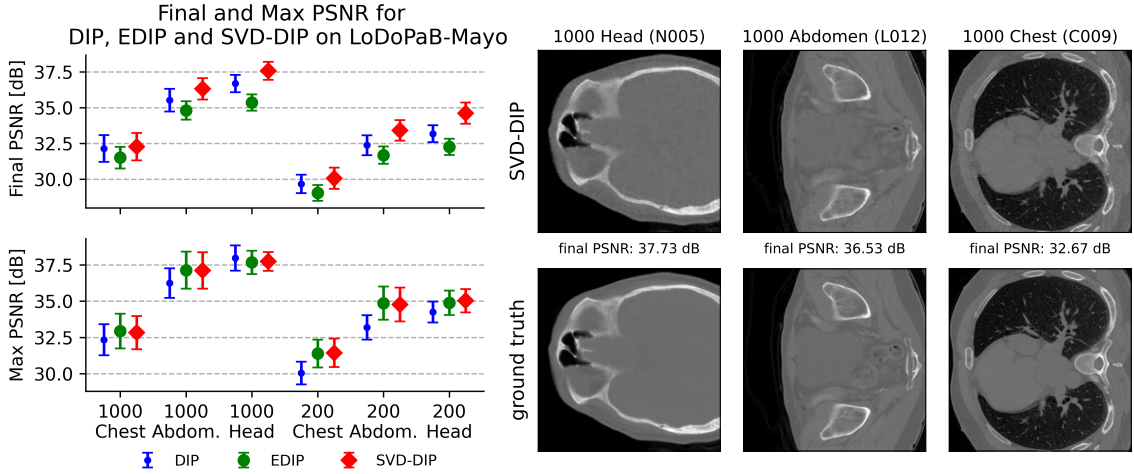


Figure 6: The mean and SD of Final and Maximum PSNR for DIP, EDIP and SVD-DIP on different body parts from LoDoPaB-Mayo, pretraining on LoDoPaB. Both 1000 and 200 angle settings are considered, indicated on the horizontal axis. For each setting, 10 samples with 3 runs each are considered. Final reconstructions of SVD-DIP are shown for the 1000 angle setting, along with the ground truth.

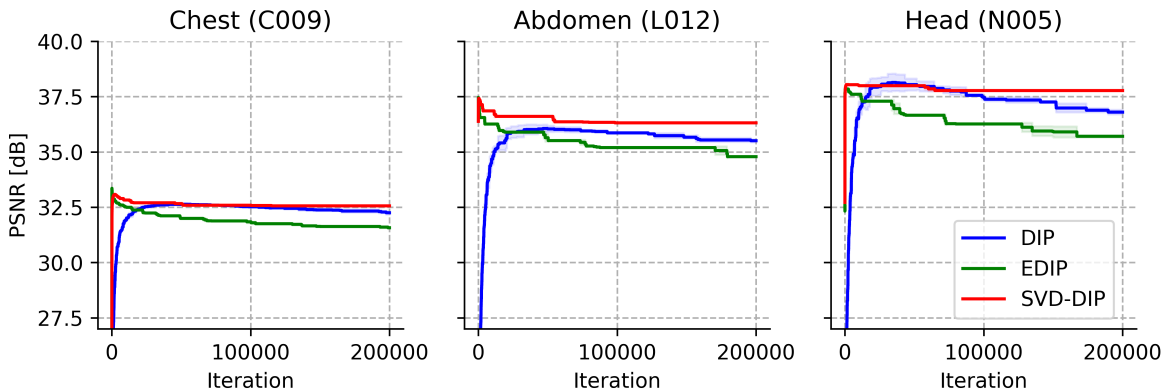


Figure 7: The mean and SD over 3 runs of the optimization of DIP, EDIP and SVD-DIP on samples from different body parts from LoDoPaB-Mayo, pretraining on LoDoPaB. The 1000 angle setting is used.

5. Conclusion

In this work we built on the regularized fine-tuning of a pretrained DIP and adopted a novel strategy that restricts the learning to the adaptation of singular values of the unfolded network parameter tensor. We proposed a variant of the DIP, named SVD-DIP, that overall overcomes the need for early stopping, but sacrifices some speed relative to EDIP. This approach yields a more stable (less prone to overfit to noise) DIP optimization. The empirical results suggest that while the SVD-DIP reconstructive properties are on par with (or slightly worse than) those of DIP or EDIP, it loses very little in terms of PSNR, even after iterating for a long time.

Acknowledgments

R.B. was supported by the i4health PhD studentship (UK EPSRC EP/S021930/1). J.L. was funded by the German Research Foundation (DFG; GRK 2224/1). The work of B.J. was partially supported by UK EPSRC grants EP/T000864/1 and EP/V026259/1. P.M. acknowledges support by DFG-NSFC project M-0187 of the Sino-German Center mobility programme.

References

- Shady Abu-Hussein, Tom Tirer, Se Young Chun, Yonina C. Eldar, and Raja Giryes. Image restoration by deep projected GSURE, 2021. URL <https://arxiv.org/abs/2102.02485>.
- Jonas Adler, Holger Kohr, Axel Ringh, Julian Moosmann, Sebastian Banert, Matthias J. Ehrhardt, Gregory R. Lee, Kati Niinimäki, Barbara Gris, Olivier Verdier, Johan Karlsson, Gustav Zickert, Willem Jan Palenstijn, Ozan Öktem, Chong Chen, Hector Andrade Loarca, and Michael Lohmann. Operator Discretization Library (ODL), 2018. *Zenodo*.

- Jonas Adler and Ozan Öktem. Solving ill-posed inverse problems using iterative deep neural networks. *Inverse Problems*, 33(12):124007, nov 2017. doi: 10.1088/1361-6420/aa9581. URL <https://doi.org/10.1088%2F1361-6420%2Faa9581>.
- Hemant Kumar Aggarwal, Aniket Pramanik, Maneesh John, and Mathews Jacob. EN-SURE: A general approach for unsupervised training of deep image reconstruction algorithms. *IEEE Transactions on Medical Imaging*, pages 1–1, 2022. doi: 10.1109/tmi.2022.3224359. URL <https://doi.org/10.1109%2Ftmi.2022.3224359>.
- Simon Arridge, Peter Maass, Ozan Öktem, and Carola-Bibiane Schönlieb. Solving inverse problems using data-driven models. *Acta Numerica*, 28:1–174, 2019. doi: 10.1017/S0962492919000059.
- Daniel Otero Baguer, Johannes Leuschner, and Maximilian Schmidt. Computed tomography reconstruction using deep image prior and learned reconstruction methods. *Inverse Problems*, 36(9):094004, sep 2020. doi: 10.1088/1361-6420/aba415. URL <https://doi.org/10.1088%2F1361-6420%2Faba415>.
- Riccardo Barbano, Johannes Leuschner, Maximilian Schmidt, Alexander Denker, Andreas Hauptmann, Peter Maass, and Bangti Jin. An educated warm start for deep image prior-based micro ct reconstruction. *IEEE Transactions on Computational Imaging*, pages 1–12, 2022. doi: 10.1109/TCI.2022.3233188.
- Tatiana A. Bubba, Andreas Hauptmann, Simo Huotari, Juho Rimpeläinen, and Samuli Siltanen. Tomographic X-ray data of a lotus root filled with attenuating objects. *Preprint, arXiv:1609.07299*, 2016.
- Thorsten M. Buzug. *Computed Tomography*, pages 311–342. Springer Berlin Heidelberg, Berlin, Heidelberg, 2011. ISBN 978-3-540-74658-4. doi: 10.1007/978-3-540-74658-4_16. URL https://doi.org/10.1007/978-3-540-74658-4_16.
- Sören Dittmer, Tobias Kluth, Peter Maass, and Daniel Otero Baguer. Regularization by architecture: a deep prior approach for inverse problems. *J. Math. Imaging Vision*, 62(3):456–470, 2020. ISSN 0924-9907. doi: 10.1007/s10851-019-00923-x. URL <https://doi.org/10.1007/s10851-019-00923-x>.
- Yonina C. Eldar. Generalized SURE for exponential families: Applications to regularization. *IEEE Transactions on Signal Processing*, 57(2):471–481, feb 2009. doi: 10.1109/tsp.2008.2008212. URL <https://doi.org/10.1109%2Ftsp.2008.2008212>.
- Heinz W. Engl, Martin Hanke, and Andreas Neubauer. *Regularization of Inverse Problems*. Kluwer Academic Publishers Group, Dordrecht, 1996. ISBN 0-7923-4157-0.
- Reinhard Heckel and Paul Hand. Deep decoder: Concise image representations from untrained non-convolutional networks. In *International Conference on Learning Representations*, 2019. URL <https://openreview.net/forum?id=rylV-2C9KQ>.
- Kazufumi Ito and Bangti Jin. *Inverse Problems: Tikhonov Theory and Algorithms*. World Scientific, Hackensack, NJ, 2015. ISBN 978-981-4596-19-0.

- Yeonsik Jo, Se Young Chun, and Jonghyun Choi. Rethinking deep image prior for denoising. In *Proceedings of the IEEE/CVF International Conference on Computer Vision (ICCV)*, pages 5087–5096, October 2021.
- Johannes Leuschner, Maximilian Schmidt, Daniel Otero Baguer, and Peter Maass. Lodopab-ct, a benchmark dataset for low-dose computed tomography reconstruction. *Scientific Data*, 8(1):109, 2021. ISSN 2052-4463. doi: 10.1038/s41597-021-00893-z. URL <https://doi.org/10.1038/s41597-021-00893-z>.
- Jiaming Liu, Yu Sun, Xiaojian Xu, and Ulugbek S. Kamilov. Image restoration using total variation regularized deep image prior, 2018. URL <https://arxiv.org/abs/1810.12864>.
- Christopher A. Metzler, Ali Mousavi, Reinhard Heckel, and Richard G. Baraniuk. Unsupervised learning with stein’s unbiased risk estimator, 2018. URL <https://arxiv.org/abs/1805.10531>.
- Taylor R. Moen, Baiyu Chen, David R. Holmes III, Xinhui Duan, Zhicong Yu, Lifeng Yu, Shuai Leng, Joel G. Fletcher, and Cynthia H. McCollough. Low-dose ct image and projection dataset. *Medical Physics*, 48(2):902–911, 2021. doi: <https://doi.org/10.1002/mp.14594>. URL <https://aapm.onlinelibrary.wiley.com/doi/abs/10.1002/mp.14594>.
- Gregory Ongie, Ajil Jalal, Richard G Baraniuk, Christopher A Metzler, Alexandros G Dimakis, and Rebecca Willett. Deep learning techniques for inverse problems in imaging. *IEEE J. Sel. Areas Inform. Theory*, 1(1):39–56, 2020.
- Olaf Ronneberger, Philipp Fischer, and Thomas Brox. U-net: Convolutional networks for biomedical image segmentation, 2015. URL <https://arxiv.org/abs/1505.04597>.
- Zenglin Shi, Pascal Mettes, Subhransu Maji, and Cees G. M. Snoek. On measuring and controlling the spectral bias of the deep image prior, 2021. URL <https://arxiv.org/abs/2107.01125>.
- Yanpeng Sun, Qiang Chen, Xiangyu He, Jian Wang, Haocheng Feng, Junyu Han, Errui Ding, Jian Cheng, Zechao Li, and Jingdong Wang. Singular value fine-tuning: Few-shot segmentation requires few-parameters fine-tuning. In *NeurIPS 2022*, 2022. URL <https://openreview.net/forum?id=LEqYZz7cZOI>.
- Dmitry Ulyanov, Andrea Vedaldi, and Victor Lempitsky. Deep image prior. *International Journal of Computer Vision*, 128(7):1867–1888, mar 2020. doi: 10.1007/s11263-020-01303-4. URL <https://doi.org/10.1007%2Fs11263-020-01303-4>.
- Wim van Aarle, Willem Jan Palenstijn, Jan De Beenhouwer, Thomas Altantzis, Sara Bals, K. Joost Batenburg, and Jan Sijbers. The ASTRA Toolbox: A platform for advanced algorithm development in electron tomography. *Ultramicroscopy*, 157:35–47, 2015. doi: <https://doi.org/10.1016/j.ultramic.2015.05.002>.
- Hengkang Wang, Taihui Li, Zhong Zhuang, Tiancong Chen, Hengyue Liang, and Ju Sun. Early stopping for deep image prior, 2021. URL <https://arxiv.org/abs/2112.06074>.

Appendix A. The Singular Value Decomposition is Sensible

While convolutions are linear and can thus be represented using a matrix for a fixed size input, these matrices are distinct from the input-size invariant matrices that we fold our tensors into. The former, for a tensor $W \in \mathbb{R}^{C_{out} \times C_{in} \times K \times K}$ are of the shape $\hat{W} \in \mathbb{R}^{C_{out} J^2 \times C_{in} J^2}$, for input images in $\mathbb{R}^{J \times J}$, while the folded matrix is of the form $W' \in \mathbb{R}^{C_{out} \times C_{in} K^2}$. For the former, it is direct that the SVD's use of matrix multiplication to compose the derived linear transformations yields the original convolution. For the latter, it is not self evident at first glance whether the multiplicative structure of the folded matrices is consistent with the composition of the convolutions they encode. Fortunately this is indeed the case in our case. The key reason for this is that we unfold into 1×1 convolutions on the left. In the following, we demonstrate this rigorously:

For any integer N , we denote by the notation $[N]$ the set $\{1, \dots, N\}$. Then for any integers N, M , (odd) K and J , let

$$\begin{aligned} W &:= (w_{n,m,k_1,k_2})_{(n,m,k_1,k_2) \in [N] \times [M] \times [K]^2} \in \mathbb{R}^{N \times M \times K \times K}, \\ X &:= (x_{m,j_1,j_2})_{(m,j_1,j_2) \in [M] \times [J]^2} \in \mathbb{R}^{M \times J \times J}, \end{aligned}$$

be two tensors. Then we can define the 2d convolution of X with W as a tensor

$$\text{conv2d}(W, X) := (y_{n,j_1,j_2})_{(n,j_1,j_2) \in [N] \times [J]^2} \in \mathbb{R}^{N \times J \times J}$$

with

$$y_{n,j_1,j_2} := \sum_{m=1}^M \sum_{k_1=1}^K \sum_{k_2=1}^K w_{n,m,k_1,k_2} \cdot X_{m,j_1+k_1-\frac{K-1}{2}-1, j_2+k_2-\frac{K-1}{2}-1}$$

with $X_{m,i_1,i_2} := 0$ when either of the indices i_1, i_2 is outside of $[J]$.

Then, for a given weight tensor $W \in \mathbb{R}^{N \times M \times K \times K}$ that can be represented by a matrix $A'B' = W' \in \mathbb{R}^{N \times MK^2}$, and a given feature map $X \in \mathbb{R}^{M \times J \times J}$, taking the 2-dimensional convolution of X with respect to W is identical to convolving X by appropriate tensor representations of $B' \in \mathbb{R}^{R \times M \cdot K \cdot K}$ and (then) $A' \in \mathbb{R}^{N \times R \cdot 1 \cdot 1}$. Note that the second tensor only codes 1×1 convolutions. To prove this result, we need the following lemma:

Lemma 1 *Let $M, K \in \mathbb{N}_{>0}$. Given a bijection between indices $f : [M] \times [K]^2 \rightarrow [MK^2]$, we can define a map that folds tensors into matrices:*

$$\begin{aligned} \Phi_f : \bigoplus_{N=1}^{\infty} \mathbb{R}^{N \times M \times K \times K} &\rightarrow \bigoplus_{N=1}^{\infty} \mathbb{R}^{N \times MK^2} \\ (x_{n,m,k_1,k_2})_{(n,m,k_1,k_2) \in [N] \times [M] \times [K]^2} &\mapsto (x_{n,f^{-1}(i)})_{(n,i) \in [N] \times [MK^2]} \end{aligned}$$

Let $g : [M] \times [K]^2 \rightarrow [MK^2]$ be a bijection, $N, R, J \in \mathbb{N}_{>0}$ be tensor dimensions, $X \in \mathbb{R}^{M \times J \times J}$ an input feature map. Let $W := (w_{n,m,k_1,k_2})_{(n,m,k_1,k_2) \in [N] \times [M] \times [K]^2} \in \mathbb{R}^{N \times M \times K \times K}$ be a tensor. Fix a bijection of indices $g : [M] \times [K]^2 \rightarrow [MK^2]$. Define $W' := \Phi_g^{-1}(W)$. Let $R \in \mathbb{N}_{>0}$, $A' \in \mathbb{R}^{N \times R}$, $B' \in \mathbb{R}^{R \times MK^2}$ such that $W' = A'B'$. Further, define $A :=$

$\Phi_{(Id_{[R]}, Id_{[1]}, Id_{[1]})}^{-1}(A')$, $B := \Phi_g^{-1}(B')$ as the "unfolded" tensors of A', B' . Let $X \in \mathbb{R}^{M \times J \times J}$ be an arbitrary tensor/feature map. Then the following identity holds

$$\text{conv2d}(W, X) = \text{conv2d}(A, \text{conv2d}(B, X)).$$

Proof We define the following tensors:

$$\begin{aligned} (a_{n,r,k_1,k_2})_{(n,r,k_1,k_2) \in [N] \times [R] \times [1] \times [1]} &:= A \\ (b_{r,m,k_1,k_2})_{(r,m,k_1,k_2) \in [R] \times [M] \times [K]^2} &:= B \\ (y_{r,j_1,j_2})_{(r,j_1,j_2) \in [R] \times [J]^2} &:= Y := \text{conv2d}(B, X) \end{aligned}$$

Further, let π_3, π_4 be the mappings that extract the third and fourth entries of a given tuple. Then the proof reduces to the following elementary argument, exploiting the linearity of the operators involved:

$$\begin{aligned} (\text{conv2d}(A, \text{conv2d}(B, X)))_{n,j_1,j_2} &= (\text{conv2d}(A, Y))_{n,j_1,j_2} \\ &= \sum_{r=1}^R \sum_{k_1=1}^1 \sum_{k_2=1}^1 a_{n,r,k_1,k_2} \cdot Y_{r,j_1+k_1-\frac{1-1}{2}-1, j_2+k_2-\frac{1-1}{2}-1} \\ &= \sum_{r=1}^R a_{n,r,1,1} \cdot Y_{r,j_1,j_2} \\ &= \sum_{r=1}^R a_{n,r,1,1} \cdot \sum_{m=1}^M \sum_{k_1=1}^K \sum_{k_2=1}^K b_{r,m,k_1,k_2} \cdot X_{m,j_1+k_1-\frac{K-1}{2}-1, j_2+k_2-\frac{K-1}{2}-1} \\ &= \sum_{r=1}^R a_{n,r} \cdot \sum_{i=1}^{MK^2} b_{r,i} \cdot X_{m,j_1+\pi_3(\Phi_g^{-1}(i))-\frac{K-1}{2}-1, j_2+\pi_3(\Phi_g^{-1}(i))-\frac{K-1}{2}-1} \\ &= \sum_{i=1}^{MK^2} \sum_{r=1}^R a_{n,r} \cdot b_{r,i} \cdot X_{m,j_1+\pi_3(\Phi_g^{-1}(i))-\frac{K-1}{2}-1, j_2+\pi_3(\Phi_g^{-1}(i))-\frac{K-1}{2}-1} \\ &= \sum_{i=1}^{MK^2} w_{n,i} \cdot X_{m,j_1+\pi_3(\Phi_g^{-1}(i))-\frac{K-1}{2}-1, j_2+\pi_3(\Phi_g^{-1}(i))-\frac{K-1}{2}-1} \\ &= \sum_{m=1}^M \sum_{k=1}^K \sum_{k_2=1}^K w_{n,m,k_1,k_2} \cdot X_{m,j_1+k_1-\frac{K-1}{2}-1, j_2+k_2-\frac{K-1}{2}-1} \\ &= (\text{conv2d}(W, X))_{n,j_1,j_2}. \end{aligned}$$

This completes the proof of the claim and hence also the lemma. ■

Note that in the statement, the embedding of A' as a tensor does not permute its indices at all, only adding two more dimensions of size 1. Meanwhile, B' is subjected to the same index transform g^{-1} as the original matrix W' .

By applying the lemma twice, first for $U' \cdot (S'V')$, then for $U' \cdot V'$, we deduce that we can replace a convolutional layer with the three induced by the SVD decomposition.

Appendix B. Experimental setup details

Python code is publicly available at https://github.com/educating-dip/svd_dip.

For the Lotus root dataset (Bubba et al., 2016), we use the forward operator matrix that has been provided with the dataset to implement fan-beam geometry. We use a TV reconstruction from all 120 angles as our ground truth reference, while our reconstruction task uses a sparse-view setting with 20 angles. The data is real-measured and thus already contains noise.

For the medical datasets, we use the ODL library (Adler et al., 2018) with the CUDA-accelerated ASTRA (van Aarle et al., 2015) backend to implement the parallel-beam geometries with 200 and 1000 angles, respectively. We simulate projections with (pre-log) Poisson noise, i.e., the full post-log model is given by

$$Ax + \nu = y, \quad \nu = -Ax - \ln(N_1/N_0), \quad N_1 \sim \text{Pois}(N_0 \exp(-Ax)),$$

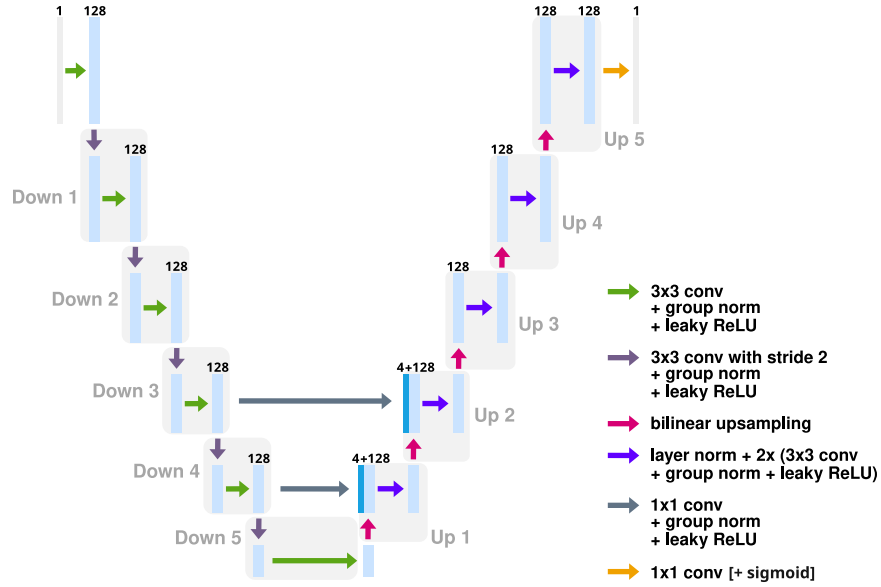
where $N_0 = 4096$ is the number of photons per detector pixel for an empty scan. Here, x denotes the linear attenuation coefficients obtained from the Hounsfield unit values x_{HU} stored in DICOM files via $x = (20 - 0.02)x_{\text{HU}}/1000 + 20$. After simulation, both images and projection data are divided by $\mu_{\text{max}} = 81.35858$ to normalize images into the range $[0, 1]$. We use the appropriate Poisson regression loss that maximizes the likelihood under this model as our data discrepancy loss,

$$L_{\text{Pois}}(A \cdot | y) = - \sum_{j=1}^m N_0 \exp(-y_j \mu_{\text{max}}) (-(A \cdot)_j \mu_{\text{max}} + \ln(N_0)) - N_0 \exp(-(A \cdot)_j \mu_{\text{max}}), \quad (2)$$

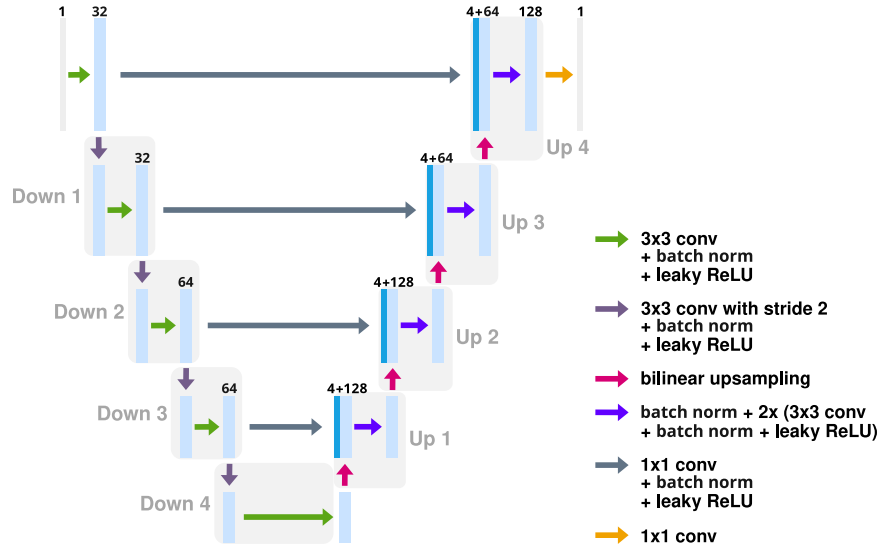
instead of the term $\|A \cdot -y\|_2^2$ in Equation 1 for all methods.

Dataset to reconstruct	Noise	Data loss	γ
Lotus root (Sparse 20)	real-measured	$\frac{1}{n} \ A \cdot -y\ _2^2$	1e-4
LoDoPaB (Sparse 200): Chest	Poisson	$L_{\text{Pois}}(A \cdot y)$	4
Mayo (Sparse 200): Chest, Abdomen, Head	Poisson	$L_{\text{Pois}}(A \cdot y)$	7
Mayo (Sparse 1000): Chest, Abdomen, Head	Poisson	$L_{\text{Pois}}(A \cdot y)$	7

Table 2: Noise type, data losses and regularization parameters used for the different datasets. The respective data loss is used in place of $\|A \cdot -y\|_2^2$ in the objective Equation 1. The same choices are used for DIP, EDIP and SVD-DIP.



(a) U-Net used for Ellipses-Lotus and Ellipses-LoDoPaB. Linear output activation is used for Ellipses-Lotus, while Ellipses-LoDoPaB uses sigmoid output activation.



(b) U-Net used for LoDoPaB-Mayo

Figure 8: U-Net architectures

Appendix C. Additional results

Table 3: PSNR values for Ellipses-Lotus (Sparse 20), 100000 Iterations.

Method	Final	Max (Iteration)	Max–Final	Final–Init
DIP	30.75	31.24 (8527)	0.4970	16.50
EDIP	30.75	31.66 (832)	0.9090	3.71
SVD-DIP (No reduction)	31.67	31.67 (94662)	0.0028	4.63
SVD-DIP (50% rd.)	31.59	31.59 (98941)	0.0027	4.83
SVD-DIP (10% thresh.)	31.65	31.65 (98339)	0.0010	5.26
SVD-DIP (50% rd. no pretraining)	27.31	27.31 (99540)	0.0000	10.58

Table 4: PSNR values for Ellipses-LoDoPaB (Sparse 200) samples, 50000 Iterations.

Test Set Index	DIP		Pretraining	EDIP		SVD-DIP	
	Final	Max	Init	Final	Max	Final	Max
6	34.81	37.77	32.6	35.07	37.62	37.24	37.28
9	30.67	34.59	30.22	30.98	34.42	33.87	33.93
11	29.69	33.93	28.65	30.55	33.6	33.05	33.11
13	36.17	39.74	35.57	36.97	39.4	38.86	38.91
17	31.63	36.39	31.12	31.81	35.85	35.29	35.45
19	31.33	34.05	30.48	31.47	33.77	33.52	33.71
22	30.56	33.46	31.14	30.97	33.33	32.86	33.04
29	32.76	36.01	31.43	32.94	35.87	35.27	35.42
34	31.47	33.06	24.76	31.4	32.84	32.73	32.85
43	31.75	34.42	29.13	31.7	34.2	33.78	33.91
Mean	32.08	35.34	30.51	32.39	35.09	34.65	34.76

Table 5: PSNR values for LoDoPaB-Mayo (Full 1000), Chest/C samples, 40000 iterations.

	DIP		Pretraining	EDIP		SVD-DIP	
Patient	Final	Max	Init	Final	Max	Final	Max
C001	33.27	33.7	23.31	32.3	34.96	33.53	34.6
C002	30.63	30.68	24.44	30.23	31.11	30.75	31.03
C004	31.97	32.03	24.01	31.49	32.57	32.07	32.42
C009	32.25	32.64	20.86	31.57	33.36	32.56	33.08
C012	31.19	31.26	25.96	30.67	32.2	31.41	32.15
C016	32.1	32.12	25.58	31.61	32.69	32.17	32.58
C019	33.63	34.1	22.11	32.66	34.5	33.84	34.54
C021	32.46	32.51	19.77	32.05	32.48	32.25	32.54
C023	30.99	31.1	23.22	30.56	31.47	31.14	31.49
C027	32.91	33.24	24.48	31.92	34.01	33.01	33.89
Mean	32.14	32.34	23.38	31.51	32.93	32.27	32.83

Table 6: PSNR values for LoDoPaB-Mayo (Sparse 200), Chest/C samples, 200000 Iterations.

	DIP		Pretraining	EDIP		SVD-DIP	
Patient	Final	Max	Init	Final	Max	Final	Max
C001	30.36	30.99	32.29	29.64	33.04	30.93	33.09
C002	28.61	28.82	29.71	28.09	30.01	28.94	30.1
C004	29.69	29.97	28.06	29.16	31.22	29.97	31.11
C009	29.78	30.26	30.17	29.08	31.63	30.27	31.76
C012	28.85	29.09	29.82	28.33	30.67	29.34	30.85
C016	29.57	29.73	28.02	29.06	30.96	29.83	31.02
C019	30.83	31.52	27.07	30.03	32.55	31.54	32.79
C021	29.89	30.07	16.45	29.24	31.12	29.94	30.85
C023	29.14	29.53	24.39	28.54	30.3	29.41	30.36
C027	30.02	30.47	31.52	29.24	32.45	30.51	32.46
Mean	29.67	30.04	27.75	29.04	31.39	30.07	31.44

Table 7: PSNR values for LoDoPaB-Mayo (Full 1000), Abdomen/L samples, 200000 Iterations.

Patient	DIP		Pretraining	EDIP		SVD-DIP	
	Final	Max	Init	Final	Max	Final	Max
L004	35.8	36.64	32.04	35.12	37.56	36.8	37.37
L006	36.66	37.91	35.32	35.44	38.7	37.44	38.81
L012	35.51	36.07	36.4	34.79	37.46	36.31	37.42
L014	36.41	37.63	36.2	35.42	39.09	37.12	38.91
L019	35.22	35.98	36.1	34.16	37.94	36.11	38.09
L024	35.93	36.52	22.22	35.43	36.55	36.63	36.63
L027	35.3	35.72	27.16	34.81	35.87	35.93	35.93
L030	34.05	34.47	23.51	33.83	35.02	34.97	35.01
L033	34.35	34.9	32.22	33.67	35.56	35.21	35.6
L035	35.97	36.53	32.23	35.33	37.54	36.65	37.33
Mean	35.52	36.24	31.34	34.8	37.13	36.32	37.11

Table 8: PSNR values for LoDoPaB-Mayo (Sparse 200), Abdomen/L samples, 200000 Iterations.

Patient	DIP		Pretraining	EDIP		SVD-DIP	
	Final	Max	Init	Final	Max	Final	Max
L004	32.91	34.04	34.39	32.12	35.25	34.25	35.52
L006	33.15	34.26	33.39	32.12	36.36	33.96	36.19
L012	32.27	32.89	34.24	31.69	35.31	33.35	35.04
L014	33.06	34.24	33.85	31.99	36.5	33.97	36.45
L019	31.7	32.76	33.83	30.92	35.26	33.01	35.35
L024	33.02	33.53	28.32	32.37	34.09	33.92	33.97
L027	32.04	32.51	30.56	31.63	33.78	32.87	33.77
L030	31.54	31.98	31.56	31.03	33.26	32.51	33.24
L033	31.16	31.94	32.32	30.58	33.17	32.1	32.9
L035	32.93	33.7	34.8	32.37	35.61	34.17	35.27
Mean	32.38	33.19	32.72	31.68	34.86	33.41	34.77

Table 9: PSNR values for LoDoPaB-Mayo (Full 1000), Head/N samples, 200000 Iterations.

	DIP		Pretraining	EDIP		SVD-DIP	
Patient	Final	Max	Init	Final	Max	Final	Max
N001	37.62	39.09	28.69	35.99	39.26	38.57	38.81
N003	35.5	36.34	17.33	34.69	36.55	36.67	36.68
N005	36.8	38.15	32.53	35.71	37.88	37.77	38.05
N012	36.36	37.28	30.5	34.86	37.4	37	37.38
N017	36.13	37.05	16.71	34.73	36.66	36.96	36.96
N021	37.02	38.22	19.35	35.78	38.07	38.04	38.04
N024	36.12	37.36	24.69	34.47	36.75	36.74	36.98
N025	36.94	38.45	26.5	35.53	37.77	37.89	38.04
N029	37.05	39.09	23.43	35.73	38.25	37.88	38.16
N030	37.26	38.6	28.94	36.05	38.11	38.11	38.2
Mean	36.68	37.96	24.87	35.35	37.67	37.56	37.73

Table 10: PSNR values for LoDoPaB-Mayo (Sparse 200), Head/N samples, 200000 Iterations.

	DIP		Pretraining	EDIP		SVD-DIP	
Patient	Final	Max	Init	Final	Max	Final	Max
N001	33.91	35.06	28.06	32.72	36.09	35.61	36.31
N003	32.32	33.04	19.9	31.34	33.04	33.49	33.56
N005	33.12	34.43	29.94	32.43	35.21	34.48	35.13
N012	32.52	33.39	27.91	31.84	34.42	33.72	34.43
N017	33.07	33.84	21.17	32.21	34.3	34.3	34.36
N021	34.03	34.99	22.86	32.77	35.39	35.77	35.84
N024	32.32	33.45	22.82	31.18	34.23	33.9	34.31
N025	33.46	34.49	25.26	32.62	35.34	34.67	35.16
N029	33.57	35.11	25.37	32.73	35.51	34.97	35.62
N030	33.46	34.69	27.91	32.77	35.34	35.18	35.51
Mean	33.18	34.25	25.12	32.26	34.89	34.61	35.02

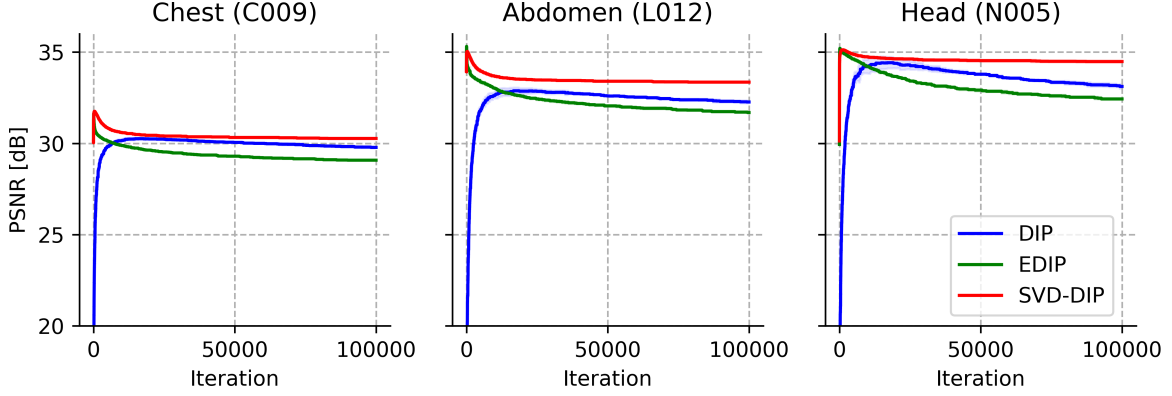


Figure 9: The mean and SD over 3 runs of the optimization of DIP, EDIP and SVD-DIP on LoDoPaB-Mayo (Sparse 200) for samples C009, L012 and N005. Each line represents the mean over 3 runs.

Appendix D. Using TV for Early Stopping

Simple strategies for early stopping (ES) are hard to come by for DIP or its variants; there is extensive literature on the subject. Most ES approaches are tailored to either a specific problem or model, and often do not generalize to different settings. For example, the interesting approach proposed by (Shi et al., 2021) requires a specialized architecture, while (Jo et al., 2021) suggest a method for ES in the context of denoising based on Stein unbiased risk estimator (SURE). First we briefly investigated whether the prior (or regulariser) could act as a proxy for an ES criterion, and discuss SURE later. Specifically we investigated whether it is possible to use the TV for ES. From Figure 10, the TV fails to yield no useful information about the PSNR curve. The TV trends upwards, with no discernible difference in this trend when the PSNR falls, making it a poor tool for predicting when overfitting occurs.

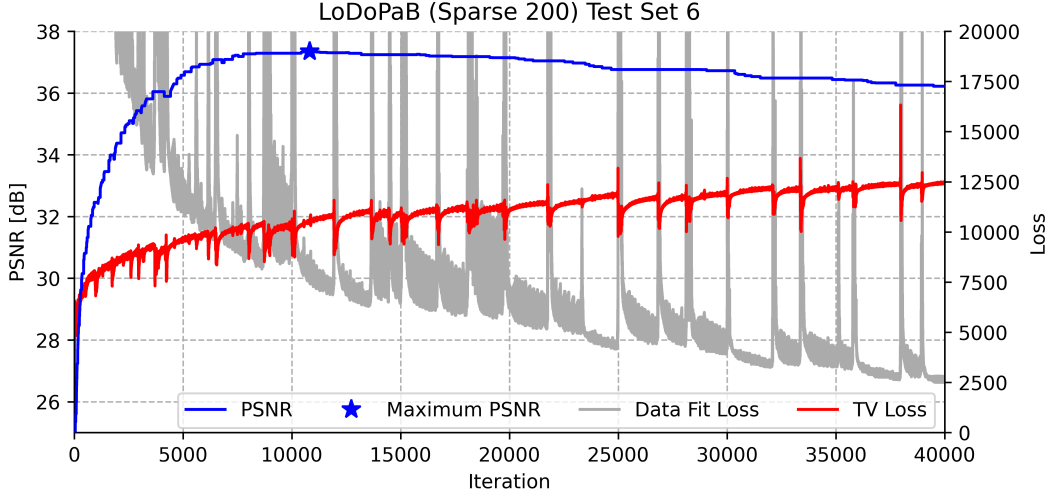


Figure 10: PSNR and mean loss output TV of DIP on LoDoPaB.

Appendix E. Is SURE a viable Method for CT?

One naturally may ask whether a DIP which utilizes Stein’s unbiased risk estimator (SURE) could serve as a better baseline than the DIP we have used. Indeed, SURE has reported state-of-the-art results on several image-restoration tasks such as de-noising, de-blurring, and super-resolution. However, we argue that its applicability to more “more ill-posed” inverse problems in imaging is currently an open field of research. Recall that the SURE is an unbiased estimate of the mean square error (MSE). Clearly, the MSE has an explicit dependence on the unknown ground truth image. In several settings, there have been very successful ways to estimate the MSE. Initially proposed by Stein for the independent, identically distributed (i.i.d.) Gaussian model, SURE has been extended to exponential distributions (GSURE) by (Eldar, 2009). Lately, GSURE has been successfully applied in the works (Metzler et al., 2018; Abu-Hussein et al., 2021; Jo et al., 2021), which have demonstrated excellent performance of the method on de-noising, de-blurring, super-resolution or, compressed sensing tasks.

In the presence of an operator, the use of SURE is less direct than for de-noising. For example, in a Gaussian linear model (e.g., $y = Ax + \nu$), the projected GSURE provides an unbiased estimate of the projected MSE, which is the expected error of the projections in the column space of the operator A . Hence, when the matrix A is rank deficient, SURE is a sub-optimal estimator as it does not estimate the orthogonal complement. Indeed, for very ill-posed inverse problems, e.g., in the highly under-sampled setting (i.e., rank-deficient setting), (Metzler et al., 2018) show that the GSURE-based projected MSE is a poor approximation of the actual MSE. To address this issue, (Aggarwal et al., 2022) propose ENSURE, which generalizes the classical SURE and GSURE formulation where the images are sampled by different operators A , chosen randomly from a set. Unfortunately, ENSURE is not applicable to CT problems in conjunction to the unsupervised DIP framework.

To confirm these observations, we run the following set of experiments. Figure 11 shows that DIP-SURE significantly outperforms DIP when optimized with the least-square

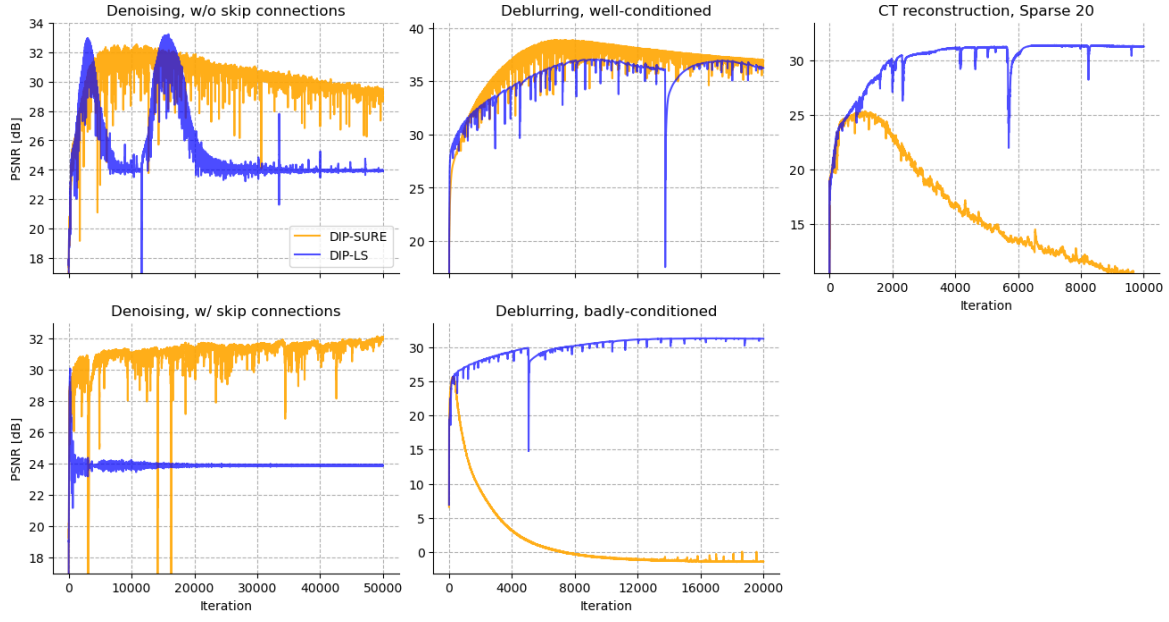


Figure 11: DIP with LS loss compared to DIP with SURE loss for different tasks on the Lotus root. For denoising (first column), we tested the network both without and with skip connections. For deblurring (second column), a well-conditioned ($\kappa(A) \sim 14$) and a badly-conditioned ($\kappa(A) \sim 1335$) problem were tested, both using skip connections in the network. For CT reconstruction (right), we use the sparse 20-angle setting like in the main experiments.

objective (DIP-LS) for the de-noising task, where we use the lotus ground truth image x and simulate the noisy image y by adding white noise $\nu \sim \mathcal{N}(0, \sigma^2 I)$ to x , with σ being half of the mean of $|x|$. The difference in the performance between DIP-SURE and DIP-LS is further accentuated if the architecture uses skips connections at every depth. Note that in the above works on SURE, all use a U-Net architecture equipped with skip connections at every depth since skip connections boost the network capacity to overfit to noise.

We then compare DIP-SURE vs. DIP-LS on Gaussian deblurring tasks. We construct two matrices A using the same Gaussian kernel but applying different Tikhonov regularization, thus adding either to the diagonal entries the mean of all diagonal entries, or 0.01 percent of the diagonal mean. This results in two blurring matrices with different condition numbers (i.e., $\kappa(A) \sim 14$ and $\kappa(A) \sim 1335$ respectively), i.e. different degree of ill-posedness. DIP-SURE outperforms DIP-LS in the mildly ill-conditioned case, whilst, as we would expect, fails on the more ill-posed task. Similarly, on the Lotus reconstruction tasks, due to ill-posedness of the reconstructive task, DIP-SURE fails to match DIP-LS. In CT reconstruction, the operator usually has very small singular values and for sparse-view scans it is also rank-deficient, rendering the problem ill-posed (Buzug, 2011). In sum, our investigation suggests that SURE is not a viable option for our setting.